

# Micromechanical investigations of CVD coated WC-Co cemented carbide by micropillar compression

Idriss El Azhari<sup>a,b,c,\*</sup>, José García<sup>d</sup>, Mohammad Zamanzade<sup>e,f</sup>, Flavio Soldera<sup>a,c</sup>, Christoph Pauly<sup>a</sup>, Christian Motz<sup>e</sup>, Luis Llanes<sup>b</sup>, Frank Mücklich<sup>a,c</sup>

<sup>a</sup> Chair of Functional Materials, Department of Materials Science, Saarland University, Campus D 3.3, D-66123, Saarbrücken, Germany

<sup>b</sup> CIEFMA - Department of Materials Science and Metallurgy, Barcelona East School of Engineering (EEBE), Universitat Politècnica de Catalunya - BarcelonaTech, E-08019, Barcelona, Spain

<sup>c</sup> Material Engineering Center Saarland (MECS), D-66123, Saarbrücken, Germany

<sup>d</sup> AB Sandvik Coromant R&D, Lerkrogsvägen 19, SE-126 80, Stockholm, Sweden

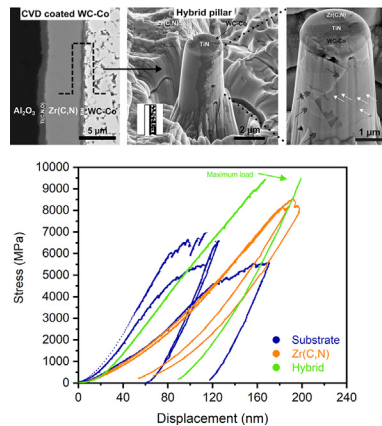
<sup>e</sup> Chair of Materials Science and Methods, Department of Materials Science, Campus D 2.2, D-66123, Saarbrücken, Germany

<sup>f</sup> Mines Saint-Etienne, University of Lyon, CNRS, UMR 5307LGF, Centre SMS, F-42023, Saint-Etienne, France

## HIGHLIGHTS

- During compression, stiffness of WC-Co micropillars is a convolution of elastic response and microplasticity events.
- Deformation of WC-Co micropillars depends on the microstructural assemblage and the distribution of both phases.
- Hybrid coating/substrate pillar shows enhanced micromechanical response, combining coating strength and substrate toughness.
- TiN interlayer provides excellent interfacial strength between the hardmetal substrate and the Zr(C,N) coating.

## GRAPHICAL ABSTRACT



## ARTICLE INFO

### Article history:

Received 24 June 2019

Received in revised form 1 September 2019

Accepted 15 October 2019

Available online 21 October 2019

### Keywords:

WC plasticity

Cobalt deformation

Zr(C,N) (ZrCN) CVD hard coating

TiN interlayer

Interfacial strength

EBSD

## ABSTRACT

Deformation behavior of an industrial coated cemented carbide (WC-Co substrate coated with CVD multilayer of TiN/Zr(C,N)/Ti(C,N,O)/Al<sub>2</sub>O<sub>3</sub>) was investigated by means of micropillar compression method. In addition to the WC-Co substrate pillars, new composite pillar combination consisting of substrate, TiN interlayer and carbonitride hard coating were tested. The study targeted to document and analyze interactions between different phases and components (substrate, interlayer and coating) while subjected to compressive stress. It is found that deformation of the substrate depends mainly on the assemblage and the distribution of WC and Co phases within the pillar. The phase assemblage is subjected to changes after deformation which has an impact on the stiffness. Detailed analysis of plastic deformation within WC coarse grains pointed out that strain energy can be extensively dissipated in this phase by means of single and multiple slip. The composite/hybrid pillar formed by association of the substrate and the coating enhanced the ultimate strength in comparison to their respective individual components, highlighting the effective load-bearing response of coating and substrate acting as a

\* Corresponding author. Chair of Functional Materials, Department of Materials Science, Saarland University, Campus D 3.3, D-66123 Saarbrücken, Germany.  
E-mail address: [idriss.elazhari@uni-saarland.de](mailto:idriss.elazhari@uni-saarland.de) (I. El Azhari).

coated system. This assessment was further supported by the excellent interfacial strength attested by the established TiN interlayer between the substrate and the coating.

© 2019 The Authors. Published by Elsevier Ltd. This is an open access article under the CC BY-NC-ND license (<http://creativecommons.org/licenses/by-nc-nd/4.0/>).

## 1. Introduction

Developing new materials combining enhanced hardness and toughness is one of the most challenging issues for material scientists and engineers. In this regard, despite the fact that they were first introduced about one century ago [1], nowadays WC-Co cemented carbide (also referred as hardmetals in practice) remains the most successful composite material combining these two properties. Main reason behind is the optimal interface properties exhibited by the WC and cobalt couple, i.e. very low interfacial energy, nearly perfect wetting and very good adhesion in the solid state [2]. Surprisingly, it has been reported that carbide-carbide interfaces are indeed strengthened by Co segregation at the grain boundaries [3]. Furthermore, mechanical properties of these materials are widely tunable by selecting the appropriate chemical and microstructural parameters, i.e. WC grain size, metallic binder volume fraction, alloying, gradients, etc. [4]. As a result, WC-Co cemented carbides have consolidated as leading materials for manufacturing tools and components used in highly demanding applications like metal cutting or forming, mining drill bits and wear parts. From the late 60s, since the implementation of thin coatings onto cemented carbides as external layers, performance and service life of cemented carbide tools and parts were taken to a higher level and have been increasingly enhanced due to the protection offered by coatings against severe wear and significant thermo-mechanical loads [5,6]. Within this context, microstructural design optimization of substrate and coatings, as well as corresponding interlayers between them, have resulted in an ever-increasing functional performance of coated hardmetals. Extensive research has been carried out to study mechanical properties of coated systems in terms of hardness, scratch resistance, friction, wear, etc. [7]. However, only a few investigations have addressed the small-scale response of these materials regarding the local mechanical properties of their individual system components, i.e. substrate, coating and interlayer. Although nanoindentation is established as a standard and popular method to characterize mechanical properties of composite materials at the micrometer scale, multi-axial stresses and strains generated during contact loading are complex [8,9]. Accordingly, studying and analyzing the involved deformation mechanics becomes very difficult. Micro-compression emerges as a more adapted method for such micromechanical characterization, considering the relative uniform stress distribution [8] and the ease of processing micropillars. Moreover, successive annular milling of the pillars with focused ion beam (FIB) allows gradual relaxation of residual stresses [10,11]. Micropillar compression could eventually be deployed for evaluating mechanical properties such as elastic modulus and yield stress. However, special care has to be given to the experimental shortcomings which can corrupt the resulting data [12]. Still, this method has been used mainly to study single crystals and single-phased materials. Micromechanical testing of WC-Co composites is limited to few studies involving either micropillar compression [13–15], microbeam bending [16,17], micro/nano-scratch testing [18,19], or in-situ tensile testing [20,21]. Regarding micropillar compression, Csanádi et al. studied the deformation dependence upon crystal orientation for WC single crystals [13]. Similar testing approach was extended to WC-Co composites by Tarragó et al. [14] and Sandoval et al. [15], aiming to highlight yielding mechanisms within the constitutive phases and microstructural scale effects, respectively. Within the present study, the same approach was used to examine deformation behavior of a lower cobalt content WC-Co coated substrate. The post-mortem deformation was investigated using high-resolution electron microscopy and EBSD to depict microstructural changes of the different phases (WC grains and Co binder).

Afterwards, micropillars milled within carbonitride coating and combined substrate/TiN-interlayer/carbonitride coating were similarly tested, and all results were compared together. In other words, complex interactions between phases (WC and Co) and different components (substrate, interlayer and coating) that likely take place under compression in real application are attempted to be replicated at the small-scale by micropillar compression. To the best knowledge of the authors, similar approach is implemented for different components of a cutting insert for the first time in this investigation. Zr(C,N) hard coating was chosen instead of the widely established Ti(C,N) due to its promising micromechanical properties [22,23], and its structural integrity when deposited on cemented carbides [24]. Besides, considering that mechanical integrity of the TiN interlayer (existing between substrate and coating) is crucial, special attention was paid to provide some insight into the interfacial strength of the system studied. Hence, the present study is divided into two main sections: investigation of deformation mechanisms of the substrate and then of the combination substrate/interlayer/coating which is here referred as a hybrid structure.

## 2. Materials and methods

### 2.1. Coated cemented carbide specimen

The investigated coated cemented carbide specimen is an industrial milling insert. It consisted of a fine grade WC-7.6 wt%Co substrate (mean carbide size of 0.8  $\mu\text{m}$ ) and a multilayer coating with the following upward sequence: TiN (0.3  $\mu\text{m}$ ), Zr(C,N) (4.5  $\mu\text{m}$ ), Ti(C,N,O) (0.6  $\mu\text{m}$ ) and  $\alpha\text{-Al}_2\text{O}_3$  (3  $\mu\text{m}$ ) as an outer layer (Fig. 1). These coatings were deposited through moderate temperature CVD process (MT-CVD) in an industrial hot wall reactor using metal chlorides precursors and temperatures ranging between 930  $^\circ\text{C}$  and 1000  $^\circ\text{C}$ . This multilayer architecture (coatings' sequence and thicknesses) is a standard sequence engineered for cemented carbides used in commercial milling inserts. The exclusive difference is the use of the recently developed Zr(C,N) wear resistant layer, instead of the widely used Ti(C,N). TiN starting interlayer is deposited on the hardmetal surface for three reasons: to promote nucleation of the carbonitride film, to act as a diffusion barrier layer and to improve adhesion to the substrate. Zr(C,N) is a hard layer intended to provide excellent combination of hardness and toughness, together with oxidation and wear resistance. Ti(C,N,O) guarantees a very good adhesion and anchoring between Zr(C,N) and alumina layer. Finally, top  $\alpha\text{-Al}_2\text{O}_3$  layer is a thermal barrier which mitigates both high heat flux generated during cutting and adhesive wear.

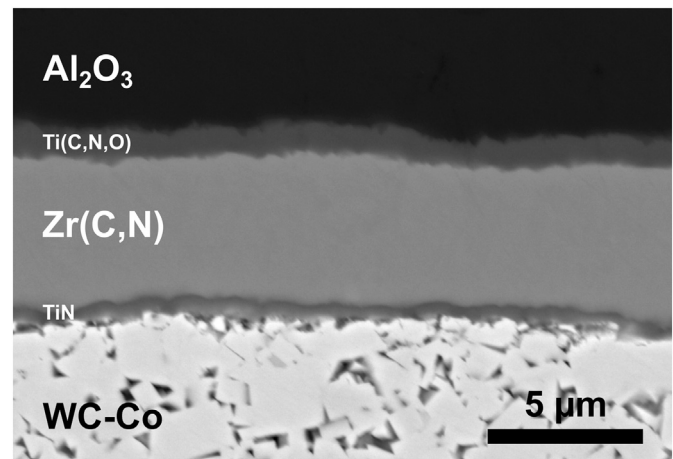


Fig. 1. Cross section of the coated cemented carbide cutting insert showing the different components.

## 2.2. Pillar preparation

Pillars were milled in an embedded cross section of the coated cemented carbide. Cross section was prepared by grinding and polishing with diamond suspension from 9 to 1  $\mu\text{m}$ . Final polishing with colloidal silica or fine alumina suspension was avoided as it has been found to produce preferential material removal in the layers, and more noticeably in the cobalt phase, which is more pronounced for fine-grained substrate grades [25]. Then, pillars were carved on the different components of the coated insert using a FEI Helios Nanolab DualBeam 600 SEM/FIB (Scanning electron microscope/Focused ion beam) operating with gallium ion ( $\text{Ga}^+$ ) beam. Three annular milling steps were conducted (with a decreasing current intensity from 21 nA, 0.92 nA and finally 0.28 nA) to achieve the final shape of the pillar with an approximate top diameter of 2  $\mu\text{m}$  and an aspect ratio (diameter/height) of 1/3. Three pillars were milled from the substrate, two from Zr(C,N) and one hybrid pillar combining substrate, TiN and Zr(C,N) coating (Table 1). Diameter and taper angle of the pillars ranged between 2.1 and 2.3  $\mu\text{m}$  and 4.4–5.5°, respectively. Besides, three additional hybrid pillars with an inclined interface were prepared in order to assess the interfacial strength of TiN interlayer (further details are given in section 3.2.2). Through the manuscript, “phases” refers to individual constituents within the substrate (WC, Co), and “components” refers to substrate, interlayer and coating.

Regarding pillar preparation, cross section orientation was adopted instead of the usual plain one for the following reasons:

- On a plain surface orientation, the hybrid pillar concept will be a top coating part based on a soft substrate, which will induce more deformation in the substrate. Besides, shear stress at the interface will be negligible.
- On the contrary, along the cross section, the substrate, the coating and their interfacial strength are tested, as the different stiffness exhibited by both components induces relevant shearing at interfaces. Moreover, with this orientation, different components can be investigated separately from the same prepared sample and within the same test. This is a clear advantage for reproducibility of the tests and comparison of the results.

## 2.3. Micro-compression tests

Micro-compression tests were carried out with the aid of a Hysitron Tribo-Indenter TI 900, equipped with a Performech controller and a 5  $\mu\text{m}$  diameter diamond flat punch. Before compression, in-situ scanning probe microscopy (SPM) of the pillar with very low force and scan rate is conducted using the flat punch as a probe. The reasons behind are to precisely locate and center the flat punch relatively to the pillar and to check misalignment. The loading function is displacement controlled with a constant rate of 5 nm/s. Maximum load of the transducer that can be applied is around 35 mN. Engineering stress (ratio of applied force to top area of the pillar) and displacement were chosen as parameters for graphical representation of mechanical response, as precise determination of the actual height was highly uncertain due to irregularities around the pillar and to the uneven nature of the pillar's base surface. Therefore, by presenting displacement instead of engineering strain such source of uncertainty and error is ruled out. Moreover, due to the tapering angle, pillars do not have perfect cylindrical shape. Hence, strain is not uniform along the pillar but rather concentrated in the upper part. Dimensions of the pillars are comparable as the same milling sequence was used. Still, small variations of heights may exist, which can influence gradually the slope of stress–displacement curves. Along the manuscript, the term “stress” refers to the “engineering stress”.

## 2.4. Residual stresses

In coated cemented carbides, two types of residual stresses may be invoked. On one hand, CVD coatings are well-known to exhibit tensile residual stresses that are balanced by the “bulk-like” substrate. However, as small specimen micropillars are machined, these residual stresses are continuously relaxed with successive annular FIB milling to a significant extent [10,11]. On the other hand, regarding cemented carbides, there exist intrinsic residual micro-stresses between co-existing phases, i.e. WC and cobalt binder. Here, it is also known that residual stresses are compressive in the ceramic phase and tensile in the metallic one. These residual stresses do not vanish completely by FIB-milling of micropillars. However, as the study is focused on cemented carbide substrate as a “single component”, such micro-residual stresses are not considered within the data analysis and beyond the scope of this investigation.

## 2.5. Electron backscattered diffraction (EBSD) analysis

Post-mortem EBSD analysis of a compressed pillar was conducted by extracting a thick lamella (~ 500 nm) with the FIB lift-out technique. Preparation protocol has been already detailed in a previous work by the authors [22]. In order to minimize possible

damage induced by the  $\text{Ga}^+$  ions employed, low current and acceleration voltage (11 pA and between 5 and 2 kV, respectively) were used during the final polishing of the lamella. Kikuchi patterns were obtained in reflection mode with an EDAX Hikari system at 20 kV acceleration voltage, 11 nA current and a 20 nm step size. Subsequently, raw data was processed and analyzed with OIM Analysis™ V7 software. It was implemented by defining a grain as an island of at least two adjacent points with a maximum misorientation of 5°. The confidence index (CI) was standardized across each grain to filter noise and poor data with a cut-off of CI = 0.09.

## 3. Results and discussion

### 3.1. Deformation of the substrate

#### 3.1.1. Stress and displacement curves

Fig. 2 shows stress vs. displacement curves of the three WC-Co pillars studied. An increase in stiffness for the first 10–20 nm of displacement is noticed. This could be attributed to tiny particles trapped between the flat punch and the pillar top face or to slight misalignment induced by height difference at the top pillar surface of a couple of nanometers. Then, during loading, the stress–displacement slope varies considerably, especially when comparing pillar S1 to pillar S3. This could be explained by considering that composite assemblage of WC grains in the Co matrix is different, regarding carbide contiguity, spatial distribution of both phases, effective grain size within the pillar and crystal orientation of carbides, in each case. As a result, each WC-Co pillar may respond to applied strain differently [14]. However, discrepancies in stress vs. displacement response during unloading, related to the elastic recovery, are not discerned. Linear data points fitting of initial unloading segment gives the following slope values of  $S_{S1} = 122 \text{ MPa/nm}$ ,  $S_{S2} = 124 \text{ MPa/nm}$  and  $S_{S3} = 128 \text{ MPa/nm}$  for pillars S1, S2 and S3, respectively.

Due to the taper angle of the pillars, strain is not uniform, but rather concentrated in the top part. Pillar S1 shows extensive and multiple yielding phenomena at the top part, given in terms of binder extrusion, relative sliding between carbide grains and slip traces of single WC grains, as shown in Fig. 3. These yielding events are translated in the stress–displacement curve, where the post-initial loading segment is non-linear and is rather a mix of this complex yielding events. Hence, the term “pseudo-stiffness” will be used instead of stiffness as the response is a mixture of elasticity and micro-plasticity events. Propensity of WC to slide, rotate or plastically deform is related to the grain size and contiguity. In general, as it is also evidenced in Fig. 3, smaller carbides tend to slide and rotate, while coarser ones are prone to deform plastically through dislocation activity [26], which is obvious due to formation of slip traces. Regarding extrusion of the metallic binder, direct linking of this deformation mechanism to features within the stress–displacement curves is very difficult, as the response is a mixture of both phases where Co is restricted to smaller regions.

For pillar S3, a significant sliding at the top is evidenced (Fig. 4 (a)). Moreover, from the rotated image in Fig. 4 (b), another line crossing the main sliding is observed, which could be an indication of multiple slip inside this grain. These events can be correlated to clear and discrete displacement bursts observed in the curves shown in Fig. 2, at stress levels of 6–7 GPa. This would be in agreement with previous results reported by Csanádi et al., regarding yield values of slip activation in monocrystalline WC pillars with comparable diameter to those studied here, during micro-compression testing [13]. The higher pseudo-stiffness and strength values, significant displacement bursts and the presumable slip activity discerned for pillar S3, triggered the interest for deeper investigations. A FIB lift-out is made for this pillar, then successive FIB cross-sectioning (according to the dashed line in Fig. 4 (b)) is carried out followed by high resolution SEM imaging. Fig. 5

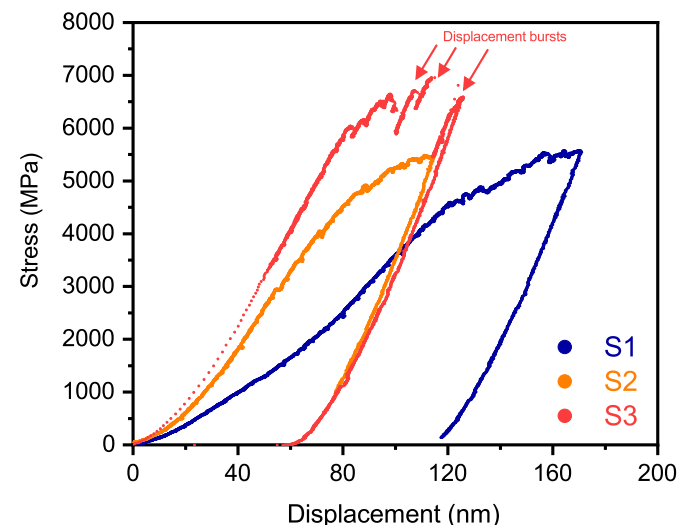
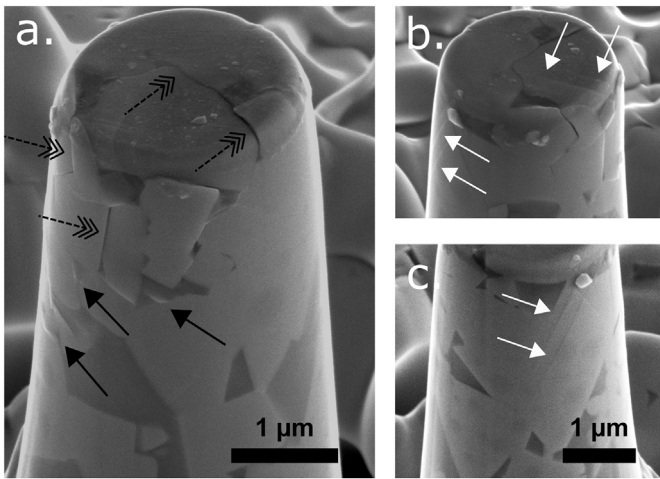


Fig. 2. Stress vs. displacement curves for substrate pillars S1, S2 and S3. Stress–displacement slope varies considerably from one pillar to another.

Table 1

Tested pillars - nomenclature used and corresponding description.

Pillar notation	Material - description
S1, S2, S3	WC-Co Substrate
C1, C2	Zr(C,N) Coatings
Hybrid (Hyb)	WC-Co/TiN/Zr(C,N) - vertical interface
Hybrid-i (Hyb-i)	WC-Co/TiN/Zr(C,N) - inclined interface



**Fig. 3.** Different views of yielding events in pillar S1 after compression. Dashed black arrows: WC sliding, black arrows: Cobalt extrusion and white arrows: Slip bands in WC.

(a) shows that the coarse WC grain in the pillar apex is supported by other WC grains, revealing then quite a high local contiguity underneath, until the base of the pillar. Hence, local assemblage could be described as a rigid continuous WC skeleton where the cobalt occupies just empty spaces between carbides. Consequently, a relatively higher pseudo-stiffness value should be expected. Aiming to gather further information, EBSD mapping was performed on multiple cross sections.

### 3.1.2. WC slip activity

To verify if the presumable slip in pillar S3 is actually related to dislocation activity or sliding at a grain boundary of two grains that would have perfect contiguity (Fig. 5 (b)), EBSD mapping was performed on several cross sections of the same lift-out. Several interesting observations can be stated. First, random and various orientations of different WC grains within the pillar are discerned in the inverse pole figure map (IPF) shown in Fig. 6 (a). From the same figure, it becomes clear that sliding at the pillar's top part occurred inside a single coarse grain, i.e. both sides neighboring slip trace exhibit same orientation (with a grain orientation spread of  $0.35^\circ$  which is close to baseline orientation noise). Second, the grain under consideration has a prismatic orientation to the plane of sectioning. In other words, the top surface of the pillar was near to parallel with the  $10\bar{1}0$  type prismatic plane which is the favorable orientation for inducing slip during compression of WC single crystals [13]. In this regard, calculating the angle between the top face of the pillar and the slip trace, an approximate value of  $130.5^\circ$  is obtained. This value is close to the angle separating two intersecting prismatic planes ( $120^\circ$ ), considering that the disorientation of the grain toward a vertical  $[10\bar{1}0]$  pole is  $11^\circ$  (Fig. 6 (c)). This means that the slip occurred likely along a prismatic plane. Confirmation to this statement is obtained by extracting exact orientation of the lattice and overlaying it to the image quality map in Fig. 6 (b), where the slip trace is parallel to the prismatic segment. Third, concerning the other crossing slip referred in Fig. 4 (b), its trace is not visible in the IQ map and calculation of the intersecting angle from the tilted view in Fig. 4 (b) is very difficult. Nevertheless, from its visible trace orientation, it seems that it probably arises from another prismatic plane of type  $0\bar{1}10$ .

In the literature, it is agreed that the predominant slip system of WC is along a prismatic plane from the family  $\{10\bar{1}0\}11\bar{2}3$  [27–30]. Other authors have also reported  $\{10\bar{1}0\}0001$  [26,31,32] and  $\{10\bar{1}0\}1120$  system [26,32] which could dissociate into  $11\bar{2}3$  partial

dislocations [32]. Calculation of the slip direction based on the geometrical measurement of the sliding from SEM pictures is not reliable, due to the difficulty of determining the lateral displacement and to the higher measurement uncertainty. Alternatively, Schmid factor maps for the  $\{10\bar{1}0\}$  slip planes were calculated (Fig. 7) for the three directions with compressive loading along the vertical axis. It appears that both  $1120$  and  $11\bar{2}3$  are very plausible directions with Schmid factor values of 0.48 and 0.38, respectively. This could lead to the conclusion that the slip took place along  $1120$  direction. However, critical resolved shear stress should be taken into account to assess which of the two directions is prone to activate first. Fig. 4 (a) shows that there is a lateral displacement during grain slip which would not take place if the slip direction was  $1120$ . This directly points out  $11\bar{2}3$  as the active slip direction in the case analyzed here.

### 3.1.3. Deformation of metallic binder, the cobalt phase

A larger EBSD scan (including the substrate below the pillar) was carried out in order to investigate the Co phase. In Fig. 8 (a), within the pillar, fcc-Co coexists mainly with small hcp-Co islands that are located near the interfaces of WC. Underneath the pillar, where the Co volume content and islands are larger, higher hcp fraction is noticed with direct contiguity to the carbides. This may suggest that phase transformation of Co begins at the interfaces with the carbides. Generally in cemented carbides, the dissolved W and C in the cobalt phase stabilize the fcc phase which is normally stable at higher temperatures [33,34]. It results in a predominance of the cubic phase [33], especially for fine-grained cemented carbides [35], which is the grade in this study. Presence of hcp-Co phase in all the mapped cross sections (e.g. Figs. 8 and 6) could lead to the impression that phase transformation occurred during micro-compression as it is well established that Co binder endures phase transformation from fcc to hcp under strain [33,34,36,37]. Nevertheless, post treatment processes like grinding [38], substrate heating during CVD deposition and cooling down, top blasting and even lamella preparation using  $\text{Ga}^+$  ion beam may also cause this phase transformation [39]. The latter factor could be discarded as precautions were adopted by using low acceleration voltage (between 5 and 2 kV) and low beam current at the final thinning step. However, the other factors could contribute to this phase transformation. Another lift-out was made at the substrate nearby pillar S3 to inspect the non-deformed state. As a result, both phases exist prior to micro-compression testing meaning that presence of hcp-Co is not strictly related to the deformation of the pillar. High resolution SEM images reveal intersecting platelet structures inside the Co island, which are reported to be related to deformation twinning and fcc-hcp martensitic phase transformation resulting in thin hcp lamellae in a fcc cobalt matrix [33,36,40]. An example is given in Fig. 5 (b) and (c) where most of the Co underneath the coarse grain is in the form of these platelet structures. Still, these structures cannot be resolved by EBSD, and the corresponding phase map in Fig. 6 (d) reveals only the fcc matrix for this particular Co island. Higher resolution technique - like transmission electron microscope (TEM) or automated crystal orientation mapping with TEM (ACOM-TEM) - could be capable of resolving these structures. At least, with pole figures shown in Fig. 8 (b), an orientation relationship between fcc and hcp phases is highlighted, where  $(0001)_{\text{hcp}} // \{111\}_{\text{fcc}}$  and  $11\bar{2}0_{\text{hcp}} // 110_{\text{fcc}}$ . This relationship has been also reported in references [33,40].

As can be seen, investigation of cobalt deformation mechanisms remains a challenge especially for low Co content and fine-grained cemented carbides due to the restricted and small Co islands. The initial allotropic phases (fcc/hcp) must be predetermined or controlled in order to assess precisely the impact of deformation on the phase transformation of Co. Various causes can induce this phase transformation and not only the applied stress during micro-compression. Nevertheless, we are assuming that phase transformation is initiated at the phase boundaries with WC grains.

### 3.1.4. Deformation mechanisms

For cemented carbide pillars, depending on the assemblage and the distribution of both WC grains and the metallic binder, distinct cases during loading stage, illustrated by pillar S1 and S3, have been demonstrated. Stress and strain concentrate at the top part as a result of the tapering angle [8]. For pillar S1 in addition to the Co flow, the upper part is composed of different WC grain sizes where the smaller ones tend to slide

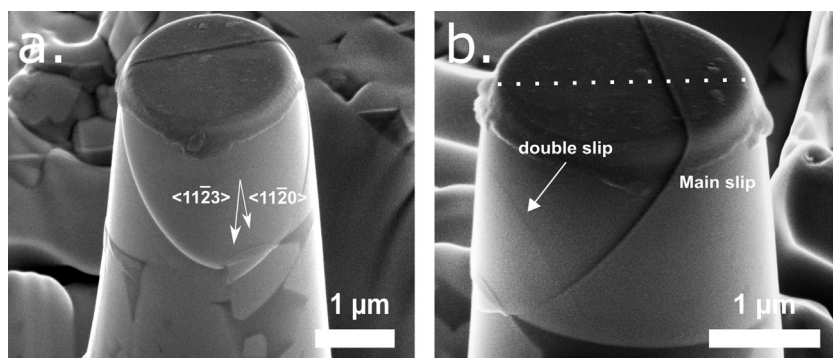


**Fig. 4.** (a) Front view of the pillar S3 after compression; (b) corresponding rotated view showing a crossing slip in WC phase. The dashed line marks the orientation of the extracted lamella which is perpendicular to the observed sliding.

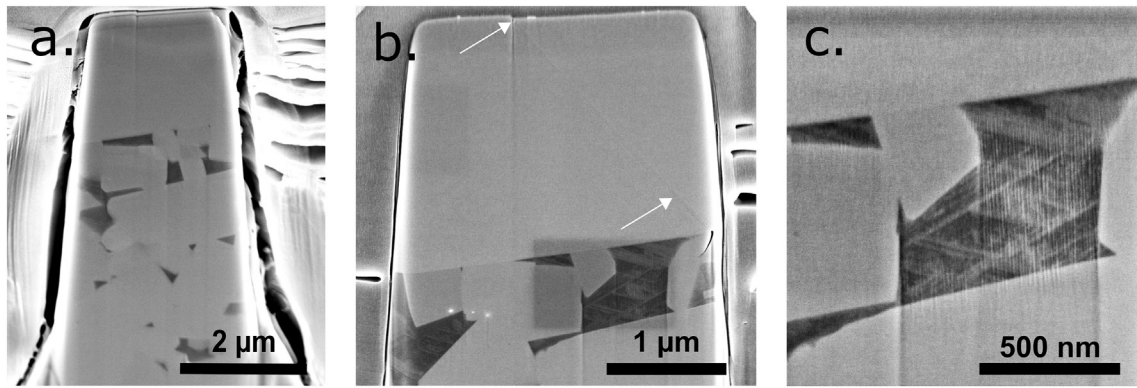


**Fig. 5.** (a) Post-mortem cross section at the middle of the pillar S3 showing a continuous WC skeleton from the top to the bottom of the pillar. (b) Another cross section showing smooth interface of the presumable slip plane in the top grain (white arrows). (c) Magnification of platelet structure inside the Co island showed in (b).

or rotate to each other considering that the interfaces (WC/WC and WC/Co) are preferential spots for plastic deformation [14,15]. Meanwhile, coarser grains tend to deform plastically by developing shear bands. The propensity to deform plastically with increasing grain size has been recently reported for WC-Co during indentation by Liu et al. [26] and it is generally related to the microstructural constraint or intrinsic size effect [41,42]. Meanwhile, the typical rigid WC skeleton of the carbides within pillar S3 resulted not only in higher pseudo-stiffness and strength, but also provided solid base for the top coarse grain that showcased extensive sliding. The latter is a result of multiple slips in prismatic planes followed by extensive shearing along the  $\{10\bar{1}0\}11\bar{2}3$  slip system which is the predominant slip system for WC [27–30]. This could be described as if a single prismatic grain was compressed on the top of the supporting WC-Co pillar structure.

However, during the unloading phase, all three pillars showed similar and higher slope than their respective loading segment. The unloading segment is related to the elastic recovery and its slope is expected to be within values of single phases [14,15] where the WC is stiffer than Co. This distinct behavior of unloading stiffness increase can be also perceived in the work of Tarragò et al. [14]. In the present case, this tendency of higher and similar unloading slopes values could be explained by the attenuation or partial annihilation of the Co phase contribution, in the overall mechanical behavior, during compression. In other words, during loading, the cobalt is significantly deformed as it is the softest phase, and for instance, Co extrusion in pillar S1 was evidenced (Fig. 3 (a)). Moreover, Co phase is dispersed and restricted to small areas between bigger and harder WC grains. These are moving and sliding along with irreversible Co deformation until the formation of

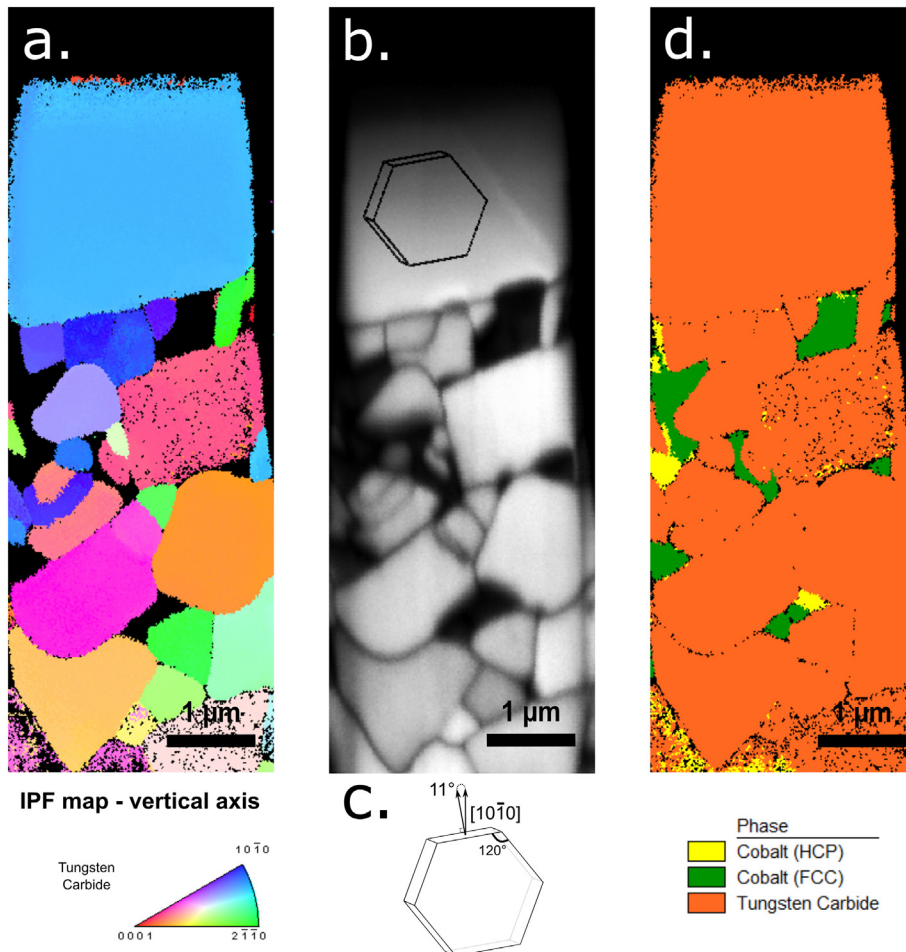


**Fig. 6.** (a) IPF map of the WC phase according to the vertical axis. (b) Corresponding image quality (IQ) map revealing that the slip trace in top grain is parallel to a prismatic plane. (c) Sketch of the disorientation angle between prismatic plane and the vertical axis. (d) WC and Co phase map.

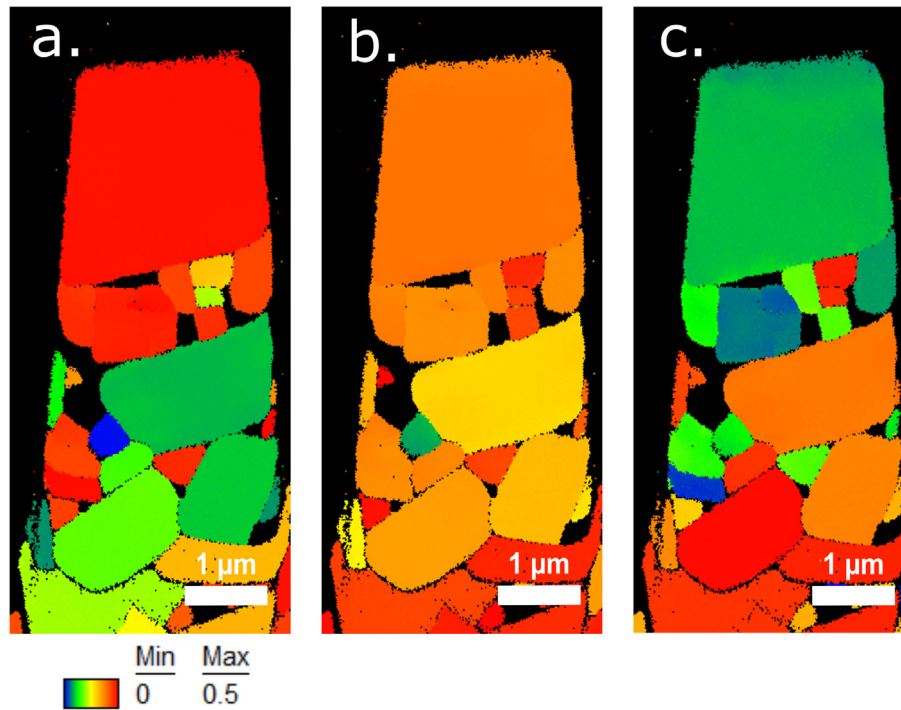


Fig. 7. Schmid factor maps of the WC phase considering the  $\{10\bar{1}0\}$  slip plane according to the following directions (a) 1120, (b) 1123 and (c) 0001.

a rigid skeleton where the WC have enough contiguity to start carrying the load and deform. As a result, the phase assemblage and contiguity will change after the compression and the elastic recovery during unloading arises mainly from WC phase.

Regarding deformation of WC and Co phases within a pillar structure (or micro-compression tests of WC-Co), in contrast to the previous study by Tarragó et al. where most of the described deformation mechanisms occurred in the Co phase and at the interfaces [14], the WC hard phase is in this study strongly concerned. This could be directly correlated to the lower cobalt content in the present study (7.6 wt% versus 15 wt%). As a result, the investigated pillars reached a higher yield strength. In Table 2, it can be observed that as the Co fraction increases the yield strength decreases and vice-versa. This would be in full accordance with what has been reported by Sandoval et al., stating that the yield strength increased with higher WC volume fraction as a result of pillar size reduction [15].

### 3.2. Deformation of coating and hybrid pillar

#### 3.2.1. Stress and displacement curves

Aiming to investigate deformation mechanisms of both coating and combined coating/substrate system, three additional pillars were produced and tested. Two of them were milled at the Zr(C,N) coating, whereas the other one was carved at the TiN interlayer between the coating and the substrate in order to get a hybrid specimen containing about the same volume fraction of both coating and cemented carbide (Fig. 9).

Stress vs. displacement curves of these pillars are shown in Fig. 10. Opposite to the mechanical response determined for substrate pillars, mechanical response of the coating is quite reproducible. The loading segments of the two coating curves are quite similar and unloading slopes are equal ( $S_{c1}=S_{c2}=79$  MPa/nm). Furthermore, a higher yield stress around 8 GPa was reached, before the first displacement burst occurred, which corresponded to crack initiation in the top face. Continuing the compression will lead to propagation of the crack along the pillar and catastrophic failure. The ultimate strength, as compared to the other components, reached the highest value in the case of the hybrid pillar. Here, stress even exceeded 9 GPa without exhibiting a displacement burst, then a plateau was reached corresponding to the maximum load that could be applied by the transducer during the micro-compression test ( $\sim 35$  mN). Post-mortem SEM images from the coating side did not reveal a visible defect or a crack formation in the coating part. Conversely, plastic deformation phenomena, such as sliding of contiguous WC grains and slip lines within individual carbides, were discerned on the substrate side as it can be seen in Fig. 11.

Given this noticeable yielding in the substrate region in contrast to the coating in addition to the dissimilar loading behavior of these two components, significant shearing is expected at both interface sides of the TiN interlayer (substrate/TiN, TiN/coating) which would lead to interfacial failure. Yet, no decohesion or interfacial crack was evidenced in our experiments which highlights the excellent bonding properties of the TiN interlayer. Instead, the whole hybrid pillar deformed as one integral structure, and both phases deformed with more leaning of the substrate part. This can be observed in Fig. 12 where SEM micrographs before and after compression were imaged with the same parameters.

Accordingly, an inclination of the pillar at the substrate part is noticed. Buckling of the pillar can be caused by stability issues related to micropillar compression. Nevertheless, precautions were adopted by having an aspect ratio between 2 and 3 in addition to the absence of excessive misalignment [43]. Moreover, as this buckling concerns only this hybrid pillar, it is obvious that the heterogeneity of the structure, where the substrate side is softer than the coating, is responsible for the observed bending.

In order to compare unloading stiffnesses between the components in Fig. 13, a rough estimate of the heights is evaluated by averaging minimum and maximum values exclusively for this purpose. It is found that the unloading stiffness of the hybrid pillar is within the values of those determined for both substrate and coating components.

To further explore the shearing resistance at the TiN interfaces, a supplementary test described below was conducted.

#### 3.2.2. Interfacial strength at the TiN interlayer

Attempting to get further insights about interfacial strength of TiN interlayer, additional three pillars were milled at a cross section near the edge of the milling insert in order to have an inclined TiN interface trapped in sandwich between the Zr(C,N) and the substrate. The idea behind is to increase the shear stresses acting at the interfaces of the TiN during compression test. Optimal case would be to have a  $45^\circ$  inclination interface to maximize the shear stress. However, due to the complicated shape of the cutting insert, it is difficult to set the sample such to get the referred angle. The latter was  $\sim 70 \pm 2^\circ$  in the present study. A larger diameter ( $\sim 3 \mu\text{m}$ ) and higher aspect ratio was chosen in order to ensure that all three components will be contained (and visible) in the pillar. Similar experimental protocols have been proposed and validated to calculate critical stress for shear failure of varied interfaces, e.g. between CrN coating and Si substrate [44] or between the matrix and the fiber of ceramic matrix composites [45]. Nevertheless, in the present study, the loading was a displacement-controlled function with a multi-cycle progressive loading, i.e. four loading-unloading cycles are applied with incremental higher displacement at each cycle. The target was to investigate occurrence of plastic deformation.

Unfortunately, before achieving pillar yielding, maximum transducer load was reached again, and the aimed critical shear stress could not be determined. Nevertheless, several important facts may be highlighted from these tests. First, failure events were not discerned at the interface. Second, as it can be seen in Fig. 14 (b), plastic deformation is taking place in the pillar after each cycle, as the loading and unloading segment are not similar. Third, "Pseudo-stiffness" is increasing after each loading cycle (Fig. 14), which is very similar to substrate pillars behavior in terms of unloading slope increase (Fig. 2). Accordingly, this result endorses the explanation about phase assemblage and contiguity changes of WC-Co after deformation (section 3.1.4). An approximation of the maximum shear stress which was exerted at the interface was calculated using the following formula [44,45]:

$$\tau = P \sin \theta \cos \theta / A$$

where  $\tau$ : shear stress, P: maximum reached load,  $\theta$ : interface angle and A: area of the pillar

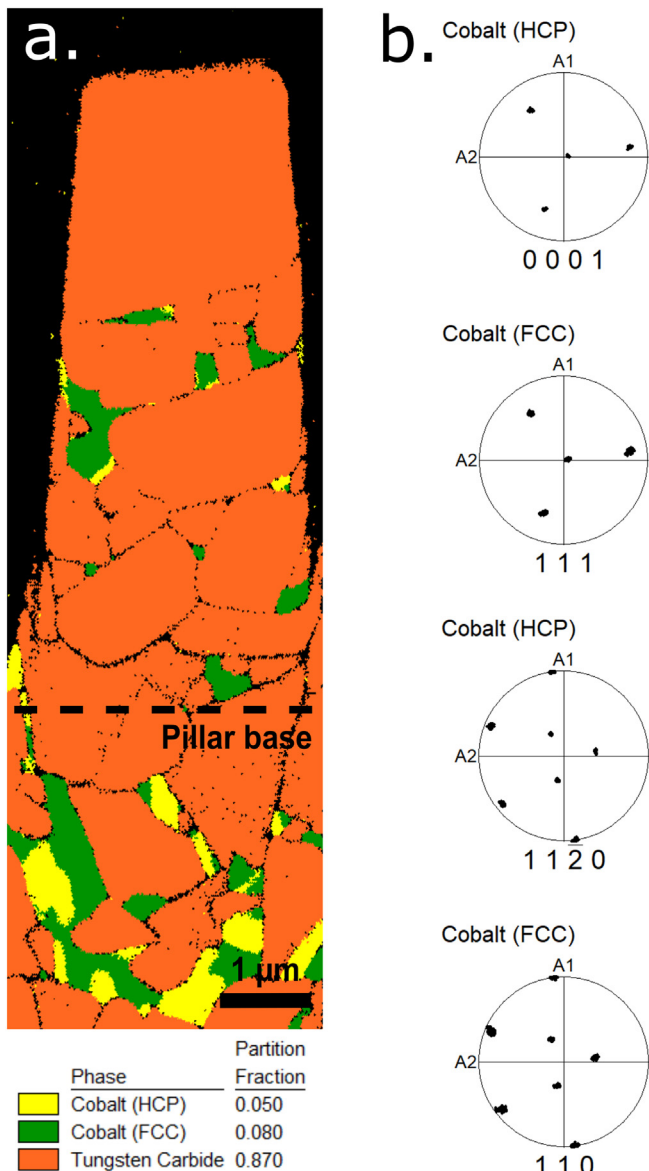


**Fig. 8.** (a) Phase map of pillar S3 and the substrate underneath. (b) Pole figures of Co fcc-hcp islands. An orientation relationship between fcc and hcp phases of cobalt is highlighted.

cross section. Estimated shear stress at the interface reached an approximate value close to 1.3 GPa, this could be taken as a lower bound estimation for its strength.

A TEM lamella was prepared in order to have a wider cross section at the TiN interface. STEM images showed absence of micro-pores or voids at TiN interfaces (Fig. 15). Furthermore, TiN presented a nanocrystalline structure with a clear contrast at the grain boundaries. This dark contrast is attributed to the segregation of diffusing substrate elements (W, Co) at the grain boundaries [23,46], which are believed to enhance the adhesion of the coating [46]. As a result of the TiN nanocrystalline microstructure, no slip transmission from the WC grains to the interface is expected.

**Table 2**

Comparison of reported WC-Co micro-compression studies. Yield strength increases inversely with Co content.

Sample	$d_{WC}$ ( $\mu m$ )	Pillar diameter ( $\mu m$ )	Yield strength (GPa)	Reference
WC-15 wt%Co	Coarse	2.5–3	0.6–3.1	[14]
WC-11 wt%Co	1.1	1–4	2.3–7	[15]
WC-7.6 wt%Co	0.8	2.1–2.3	4–7	Present study
WC (single crystal)	-	2	6–7	[13]

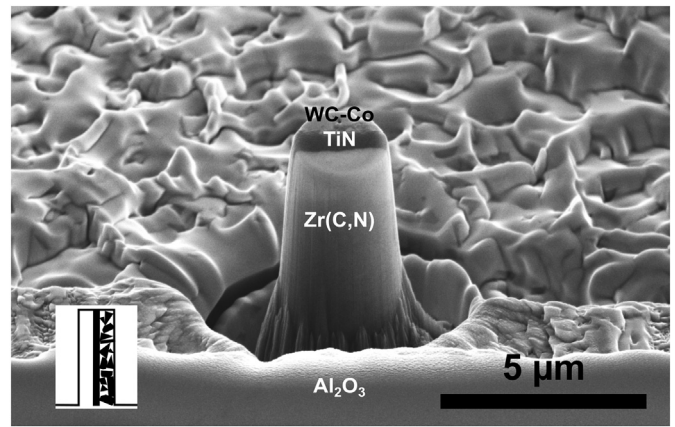


**Fig. 9.** Hybrid pillar carved at the interface with similar volume fraction of coating and substrate components. Inset: scheme of the components of the hybrid pillar showing (from left to right) Zr(C,N) coating, TiN interlayer and WC-Co substrate.

### 3.2.3. Strength of hybrid assemblage

The combination of coating and substrate outperformed their corresponding single component. It was seen that deformation of substrate pillars is ductile, contrary to coating one which is brittle. The hybrid pillar reached stresses as high as 9.4 GPa without showing a displacement burst and could probably advance to a superior strength if the transducer had a higher maximum load limit. The three components have deformed together, WC grains in the substrate deformed plastically, whereas the TiN and the Zr(C,N) hard coating bended with the substrate without developing a visible crack. Attention must be drawn to the fact that hybrid pillars behavior also depends on the assemblage of the substrate part. In the present case, like substrate pillar S3, coarse-grained assemblage and higher contiguity of WC grains were in favor for this superior behavior. From the coating perspective, this outstanding result could be attributed to the better cohesive strength (at grain boundaries) and ductility of Zr(C,N) in comparison with the widely used Ti(C,N) coating [22,23]. Indeed, it has to be taken into account that finer microstructure of Zr(C,N) along with TiN (within the hybrid pillar) increased volume fraction of grain boundaries in which substrate elements are segregating, and this feature may contribute to the increased strength [48]. Regarding the interfaces, no crack was evidenced at the interfaces of both components with TiN, which is a proof of the excellent interfacial strength that the TiN is guaranteeing between the cemented carbide and the hard coating. In fact, it has been reported that the addition of TiN interlayer has enhanced the adhesion strength between Ti(C,N) coating and WC-Co coating during cutting tests [46].

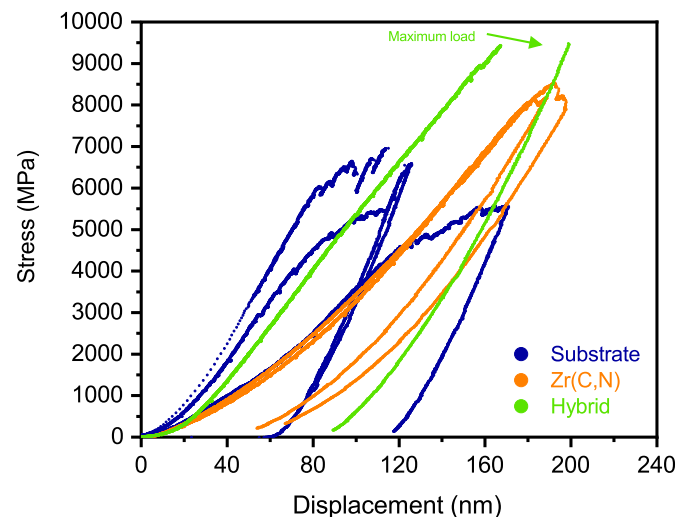


**Fig. 10.** Stress and displacement curves of substrate pillars (S1, S2, S3) (Yield strength ~ 4–7 GPa), Zr(C,N) coating pillars (Yield strength ~ 8 GPa), and hybrid pillar (Ultimate strength ~ 9 GPa). The plateau noticed for the hybrid pillar (green curve) is a result of reaching the maximum load of the transducer. Hybrid pillar exhibits highest strength among tested specimens. (For interpretation of the references to colour in this figure legend, the reader is referred to the Web version of this article.)

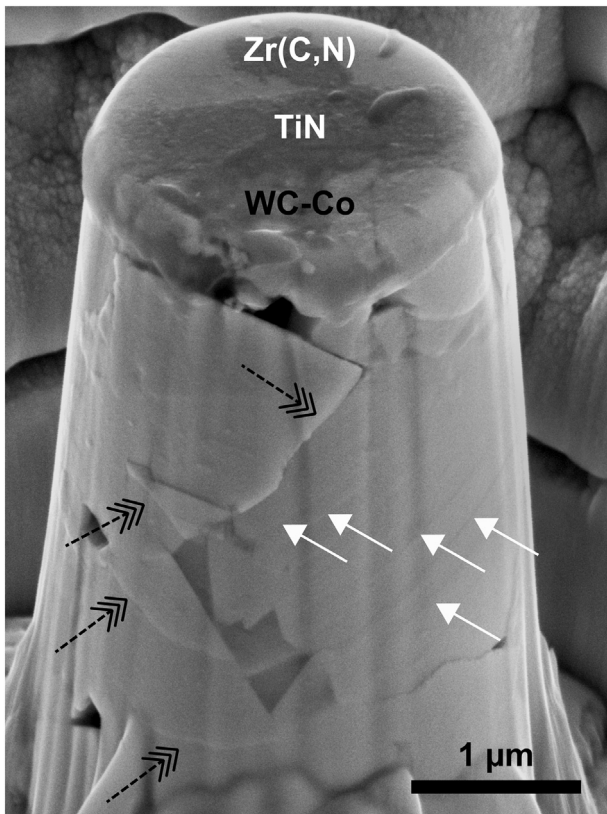


Fig. 11. Yielding events at the substrate region of the hybrid pillar, white arrows indicate slip bands in WC while black dashed ones show sliding between WC grains.

#### 4. Summary

Throughout various experiments and characterization techniques the deformation mechanisms of different components of an industrial cutting insert have been investigated, the following conclusions were drawn regarding our experiments:

- Deformation of WC-Co micropillars prepared from the same substrate is strongly influenced by phase assemblage and distribution, grain size and orientation, nature of interfaces, etc., as we obtained distinct behavior during the loading of each pillar. The loading segment (or pseudo-stiffness) is a convolution of elastic response and microplasticity events. Moreover, loading and unloading behavior were dissimilar which could be explained by the local changes in phase assemblage at the end of loading segment resulting in a stiffness increase.
- In addition to the Co metallic phase, coarse WC grains can absorb considerable strain energy by deforming plastically as it has been showcased - in one example - by the extensive and multiple slip according to the established  $\{10\bar{1}0\}11\bar{2}3$  system and initiation of several slip traces in different WC grains for the other examples.
- Investigation of cobalt phase deformation is challenging especially for low Co content and fine-grained cemented carbides. At least, we are assuming that phase transformation from fcc to hcp is initiated at the phase boundaries with WC grains.
- The hybrid pillar presented the highest strength among the tested pillars, the coating contributed with its strength while the substrate provided the necessary toughness, which enhanced its properties and outscored their individual phases in terms of ultimate strength.
- Despite high shear stresses expected at interfaces of TiN interlayer during compression, the latter provided excellent interfacial strength between the substrate and the coating, which strengthen and bind both components together.

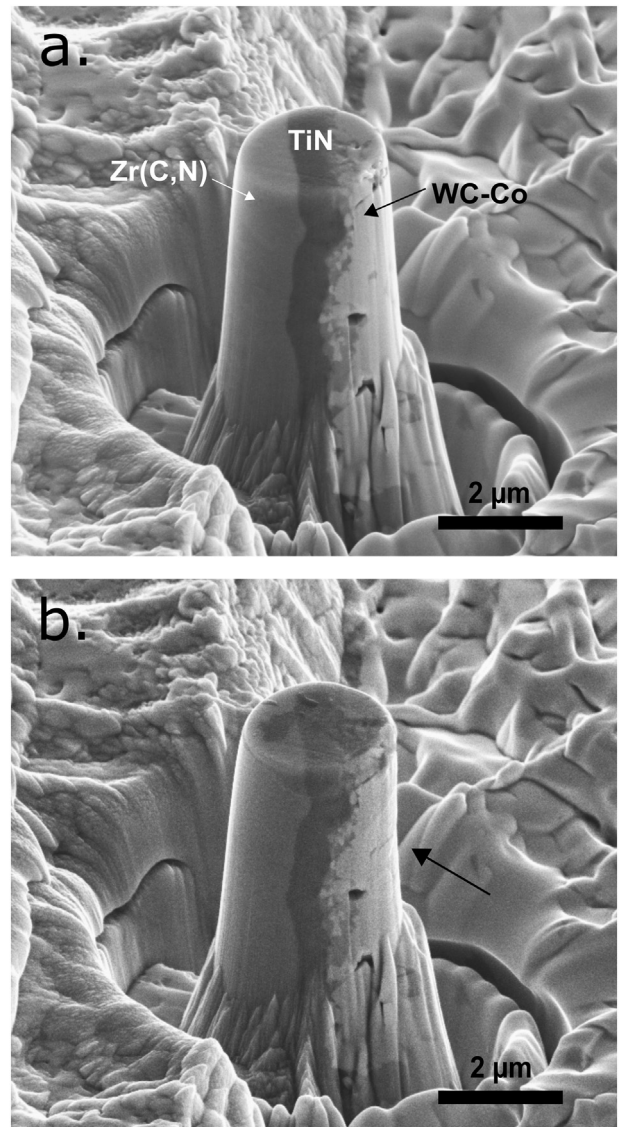


Fig. 12. (a) Side image of the hybrid pillar before compression. (b) Related post-compression image. Black arrow in (b) indicates yielding at the substrate side and leaning of the pillar to the right. This can be noticed also by taking the background surrounding the top part as a reference.

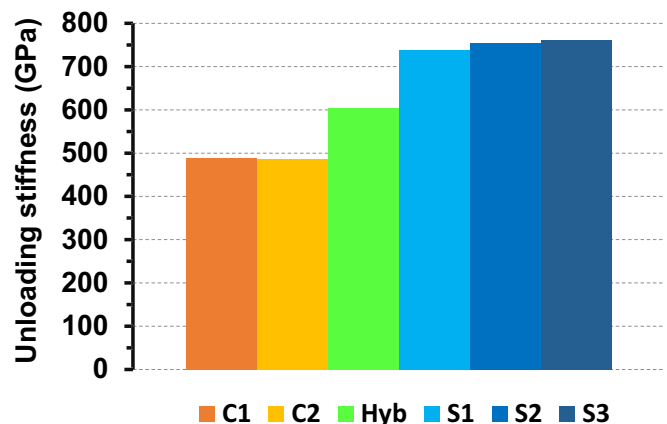
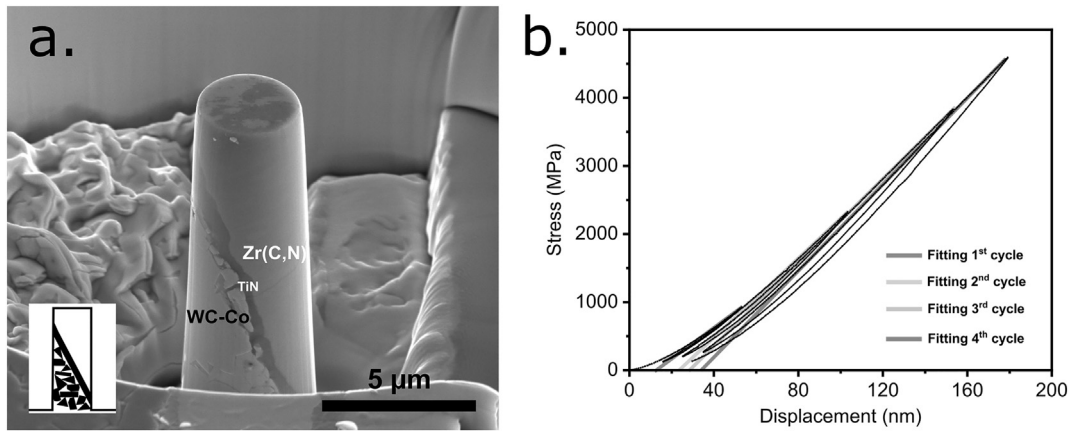


Fig. 13. Unloading stiffnesses of tested pillars, C: Coating – S: Substrate – Hyb: Hybrid. Unloading stiffness of the hybrid pillar is within the values of the corresponding components.



**Fig. 14.** a. Hybrid pillar with inclined interface (Hyb-i) after compression. Inset: scheme of the hybrid pillar with an inclined interface. b. Corresponding multi-cycle stress-displacement curve highlighting plastic deformation after each cycle. Fitting of the loading's linear part is added for each cycle. Corresponding slopes are: 1<sup>st</sup> cycle = 22.4 MPa/nm; 2<sup>nd</sup> cycle = 29.3 MPa/nm; 3<sup>rd</sup> cycle = 30.9 MPa/nm; 4<sup>th</sup> cycle = 32 MPa/nm.

### Data availability statement

The raw/processed data required to reproduce these findings cannot be shared at this time as the data also forms part of an ongoing study.

### CRediT authorship contribution statement

**Idriss El Azhari:** Conceptualization, Methodology, Investigation, Formal analysis, Visualization, Writing - original draft, Writing - review & editing. **José García:** Funding acquisition, Project administration, Resources, Supervision, Writing - review & editing. **Mohammad Zamanzade:** Conceptualization, Investigation, Validation, Writing - review & editing. **Flavio Soldara:** Funding acquisition, Project administration, Investigation, Writing - review & editing. **Christoph Pauly:** Methodology, Investigation, Validation, Writing - review & editing. **Christian Motz:** Resources, Validation, Writing - review & editing. **Luis Llanes:** Project administration, Supervision, Methodology, Validation, Writing - original draft, Writing - review & editing. **Frank Mücklich:** Funding acquisition, Project administration, Resources, Supervision, Writing - review & editing.

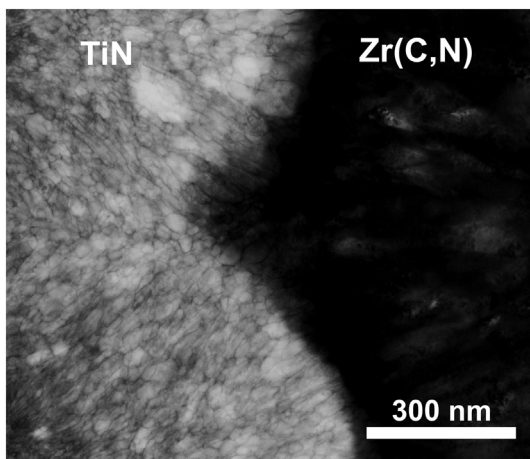


**Fig. 15.** Bright field STEM-in-SEM image at the TiN interface of the as-deposited state. TiN (left) and Zr(C,N) (right). Dark contrast around TiN grain boundaries denotes segregation of diffused substrate elements. Initial stages of the CVD deposition produce normally a fine-grained microstructure, and grain size will increase as the thickness increases [47].

### Acknowledgement

Dr. Jeanette Persson (AB Sandvik Coromant R&D) is acknowledged for producing the coated specimens. The authors deeply acknowledge X-ray measurements performed by Sebastian Slawik (Saarland university). Dr. Florian Schäfer (Saarland University) is thanked for AFM measurements. Michael Engstler (Saarland University) is thanked for the help with image analysis. The European Commission is acknowledged for funding through the projects: Erasmus Mundus Doctoral Programme DocMASE, RISE Project CREATE-Network (No 644013) and EFRE project AME-Lab (European Regional Development Fund C/4-EFRE-13/2009/Br). AB Sandvik Coromant is acknowledged for the partial financial support of the PhD thesis (Idriss El Azhari). We acknowledge support by the Deutsche Forschungsgemeinschaft (DFG, German Research Foundation) and Saarland University within the funding programme Open Access Publishing.

### References

- [1] H.M. Ortner, P. Ettmayer, H. Kolaska, I. Smid, The history of the technological progress of hardmetals, *Int. J. Refract. Metals Hard Mater.* 49 (2015) 3–8, <https://doi.org/10.1016/j.jrmhm.2014.04.016>.
- [2] H.E. Exner, Physical and chemical nature of cemented carbides, *Int. Met. Rev.* 24 (1979) 149–173, <https://doi.org/10.1179/imtr.1979.24.1.149>.
- [3] M. Christensen, G. Wahnström, Effects of cobalt intergranular segregation on interface energetics in WC-Co, *Acta Mater.* 52 (2004) 2199–2207, <https://doi.org/10.1016/j.actamat.2004.01.013>.
- [4] J. García, V. Collado Ciprés, A. Blomqvist, B. Kaplan, Cemented carbide microstructures: a review, *Int. J. Refract. Metals Hard Mater.* 80 (2019) 40–68, <https://doi.org/10.1016/j.jrmhm.2018.12.004>.
- [5] S. Söderberg, M. Sjöstrand, B. Ljungberg, Advances in coating technology for metal cutting tools, *Met. Powder Rep.* 56 (2001) 24–30, [https://doi.org/10.1016/S0026-0657\(01\)80174-0](https://doi.org/10.1016/S0026-0657(01)80174-0).
- [6] K. Bobzin, High-performance coatings for cutting tools, *CIRP J. Manuf. Sci. Technol.* 18 (2017) 1–9, <https://doi.org/10.1016/j.cirpj.2016.11.004>.
- [7] K.-D. Bouzakis, N. Michailidis, G. Skordaris, E. Bouzakis, D. Biermann, R. M'Saoubi, Cutting with coated tools: coating technologies, characterization methods and performance optimization, *CIRP Ann* 61 (2012) 703–723, <https://doi.org/10.1016/j.cirp.2012.05.006>.
- [8] H. Fei, A. Abraham, N. Chawla, H. Jiang, Evaluation of micro-pillar compression tests for accurate determination of elastic-plastic constitutive relations, *J. Appl. Mech.* 79 (2012), 061011.
- [9] M. Zamanzade, J.R. Velayarce, O.T. Abad, C. Motz, A. Barnoush, Mechanical behavior of iron aluminides: a comparison of nanoindentation, compression and bending of micropillars, *Mater. Sci. Eng. A* 652 (2016) 370–376, <https://doi.org/10.1016/j.msea.2015.11.088>.
- [10] A.M. Korsunsky, M. Sebastiani, E. Bemporad, Focused ion beam ring drilling for residual stress evaluation, *Mater. Lett.* 63 (2009) 1961–1963, <https://doi.org/10.1016/j.matlet.2009.06.020>.
- [11] M. Sebastiani, C. Eberl, E. Bemporad, G.M. Pharr, Depth-resolved residual stress analysis of thin coatings by a new FIB-DIC method, *Mater. Sci. Eng. A* 528 (2011) 7901–7908, <https://doi.org/10.1016/j.msea.2011.07.001>.
- [12] G. Dehm, B.N. Jaya, R. Raghavan, C. Kirchlechner, Overview on micro- and nanomechanical testing: new insights in interface plasticity and fracture at small length

- scales, *Acta Mater.* 142 (2018) 248–282, <https://doi.org/10.1016/j.actamat.2017.06.019>.
- [13] T. Csanádi, M. Břanda, A. Duszová, N.Q. Chinh, P. Szommer, J. Dusza, Deformation characteristics of WC micropillars, *J. Eur. Ceram. Soc.* 34 (2014) 4099–4103, <https://doi.org/10.1016/j.jeurceramosc.2014.05.045>.
- [14] J.M. Tarragó, J.J. Roa, E. Jiménez-Piqué, E. Keown, J. Fair, L. Llanes, Mechanical deformation of WC-Co composite micropillars under uniaxial compression, *Int. J. Refract. Metals Hard Mater.* 54 (2016) 70–74, <https://doi.org/10.1016/j.ijrmhm.2015.07.015>.
- [15] D.A. Sandoval, A. Rinaldi, J.M. Tarragó, J.J. Roa, J. Fair, L. Llanes, Scale effect in mechanical characterization of WC-Co composites, *Int. J. Refract. Metals Hard Mater.* 72 (2018) 157–162, <https://doi.org/10.1016/j.ijrmhm.2017.12.029>.
- [16] M. Trueba, A. Aramburu, N. Rodríguez, I. Iparraguirre, M.R. Elizalde, I. Ocaña, J.M. Sánchez, J.M. Martínez-Esnaola, “In-situ” mechanical characterisation of WC-Co hardmetals using microbeam testing, *Int. J. Refract. Metals Hard Mater.* 43 (2014) 236–240, <https://doi.org/10.1016/j.ijrmhm.2013.12.005>.
- [17] M.R. Elizalde, I. Ocaña, J. Alkorta, J.M. Sánchez-Moreno, Mechanical strength assessment of single WC-WC interfaces present in WC-Co hardmetals through microbeam bending experiments, *Int. J. Refract. Metals Hard Mater.* 72 (2018) 39–44, <https://doi.org/10.1016/j.ijrmhm.2017.12.009>.
- [18] M. Gee, K. Mingard, B. Roebuck, Application of EBSD to the evaluation of plastic deformation in the mechanical testing of WC/Co hardmetal, *Int. J. Refract. Metals Hard Mater.* 27 (2009) 300–312, <https://doi.org/10.1016/j.ijrmhm.2008.09.003>.
- [19] T. Csanádi, M. Novák, A. Naughton-Duszová, J. Dusza, Anisotropic nanoscratch resistance of WC grains in WC-Co composite, *Int. J. Refract. Metals Hard Mater.* 51 (2015) 188–191, <https://doi.org/10.1016/j.ijrmhm.2015.03.005>.
- [20] T. Namazu, T. Morikaku, H. Akamine, T. Fujii, K. Kuroda, Y. Takami, Mechanical reliability of FIB-fabricated WC-Co cemented carbide nanowires evaluated by MEMS tensile testing, *Eng. Fract. Mech.* 150 (2015) 126–134, <https://doi.org/10.1016/j.engfracmech.2015.07.007>.
- [21] X. Liu, H. Wang, L. Wang, C. Hou, X. Song, X. Liu, X. Han, In situ study of fracture behavior of ultrafine WC-Co cemented carbide, *Mater. Res. Lett.* 5 (2017) 55–60, <https://doi.org/10.1080/21663831.2016.1208300>.
- [22] I. El Azhari, J. García, M. Zamanzade, F. Soldera, C. Pauly, L. Llanes, F. Mücklich, Investigations on micro-mechanical properties of polycrystalline Ti(C,N) and Zr(C,N) coatings, *Acta Mater.* 149 (2018) 364–376, <https://doi.org/10.1016/j.actamat.2018.02.053>.
- [23] I. El Azhari, J. Barrirero, J. García, F. Soldera, L. Llanes, F. Mücklich, Atom Probe Tomography investigations on grain boundary segregation in polycrystalline Ti(C,N) and Zr(C,N) CVD coatings, *Scr. Mater.* 162 (2019) 335–340, <https://doi.org/10.1016/j.scriptamat.2018.11.041>.
- [24] I. El Azhari, J. García, F. Soldera, S. Suarez, E. Jiménez-Piqué, F. Mücklich, L. Llanes, Contact damage investigation of CVD carbonitride hard coatings deposited on cemented carbides, *Int. J. Refract. Metals Hard Mater.* (2019) 105050, <https://doi.org/10.1016/j.ijrmhm.2019.105050>.
- [25] K.P. Mingard, B. Roebuck, J. Marshall, G. Sweetman, Some aspects of the structure of cobalt and nickel binder phases in hardmetals, *Acta Mater.* 59 (2011) 2277–2290, <https://doi.org/10.1016/j.actamat.2010.12.004>.
- [26] X. Liu, J. Zhang, C. Hou, H. Wang, X. Song, Z. Nie, Mechanisms of WC plastic deformation in cemented carbide, *Mater. Des.* 150 (2018) 154–164, <https://doi.org/10.1016/j.jmatdes.2018.04.025>.
- [27] S.B. Luyckx, Slip system of tungsten carbide crystals at room temperature, *Acta Metall.* 18 (1970) 233–236, [https://doi.org/10.1016/0001-6160\(70\)90028-3](https://doi.org/10.1016/0001-6160(70)90028-3).
- [28] M.K. Hibbs, R. Sinclair, Room-temperature deformation mechanisms and the defect structure of tungsten carbide, *Acta Metall.* 29 (1981) 1645–1654, [https://doi.org/10.1016/0001-6160\(81\)90047-X](https://doi.org/10.1016/0001-6160(81)90047-X).
- [29] V. Jayaram, R. Sinclair, D.J. Rowcliffe, Intergranular cracking in WC-6% Co: an application of the von mises criterion, *Acta Metall.* 31 (1983) 373–378, [https://doi.org/10.1016/0001-6160\(83\)90214-6](https://doi.org/10.1016/0001-6160(83)90214-6).
- [30] T. Csanádi, M. Břanda, N.Q. Chinh, P. Hvizdoš, J. Dusza, Orientation-dependent hardness and nanoindentation-induced deformation mechanisms of WC crystals, *Acta Mater.* 83 (2015) 397–407, <https://doi.org/10.1016/j.actamat.2014.09.048>.
- [31] J.D. Bolton, M. Redington, Plastic deformation mechanisms in tungsten carbide, *J. Mater. Sci.* 15 (1980) 3150–3156, <https://doi.org/10.1007/BF00550388>.
- [32] T. Takahashi, E.J. Freise, Determination of the slip systems in single crystals of tungsten monocarbide, *Philos. Mag.* 12 (1965) 1–8, <https://doi.org/10.1080/14786436508224941>.
- [33] V.K. Sarin, T. Johannesson, On the deformation of WC-Co cemented carbides, *Met. Sci.* 9 (1975) 472–476, <https://doi.org/10.1179/030634575790444531>.
- [34] B. Roebuck, E.A. Almond, A.M. Cottenden, The influence of composition, phase transformation and varying the relative F.C.C. and H.C.P. phase contents on the properties of dilute Co-W-C alloys, *Mater. Sci. Eng.* 66 (1984) 179–194, [https://doi.org/10.1016/0025-5416\(84\)90179-4](https://doi.org/10.1016/0025-5416(84)90179-4).
- [35] J.M. Marshall, M. Giraudel, The role of tungsten in the Co binder: effects on WC grain size and hcp-fcc Co in the binder phase, *Int. J. Refract. Metals Hard Mater.* 49 (2015) 57–66, <https://doi.org/10.1016/j.ijrmhm.2014.09.028>.
- [36] C.H. Vassel, A.D. Krawitz, E.F. Drake, E.A. Kenik, Binder deformation in WC-(Co, Ni) cemented carbide composites, *Metall. Trans. A.* 16 (1985) 2309–2317, <https://doi.org/10.1007/BF02670431>.
- [37] U. Schleinkofer, H.-G. Sockel, K. Götting, W. Heinrich, Microstructural processes during subcritical crack growth in hard metals and cermets under cyclic loads, *Mater. Sci. Eng. A* 209 (1996) 103–110, [https://doi.org/10.1016/0921-5093\(95\)10098-9](https://doi.org/10.1016/0921-5093(95)10098-9).
- [38] J. Yang, J.J. Roa, M. Schwind, M. Odén, M.P. Johansson-Jöesaar, L. Llanes, Grinding-induced metallurgical alterations in the binder phase of WC-Co cemented carbides, *Mater. Char.* 134 (2017) 302–310, <https://doi.org/10.1016/j.matchar.2017.11.004>.
- [39] H.G. Jones, A.P. Day, D.C. Cox, Electron backscatter diffraction studies of focused ion beam induced phase transformation in cobalt, *Mater. Char.* 120 (2016) 210–219, <https://doi.org/10.1016/j.matchar.2016.09.004>.
- [40] X. Wu, N. Tao, Y. Hong, G. Liu, B. Xu, J. Lu, K. Lu, Strain-induced grain refinement of cobalt during surface mechanical attrition treatment, *Acta Mater.* 53 (2005) 681–691, <https://doi.org/10.1016/j.actamat.2004.10.021>.
- [41] E. Arzt, Size effects in materials due to microstructural and dimensional constraints: a comparative review, *Acta Mater.* 46 (1998) 5611–5626.
- [42] J.R. Greer, J.Th.M. De Hosson, Plasticity in small-sized metallic systems: intrinsic versus extrinsic size effect, *Prog. Mater. Sci.* 56 (2011) 654–724, <https://doi.org/10.1016/j.pmatsci.2011.01.005>.
- [43] H. Zhang, B.E. Schuster, Q. Wei, K.T. Ramesh, The design of accurate micro-compression experiments, *Scr. Mater.* 54 (2006) 181–186, <https://doi.org/10.1016/j.scriptamat.2005.06.043>.
- [44] Y. Mu, X. Zhang, J.W. Hutchinson, W.J. Meng, Measuring critical stress for shear failure of interfacial regions in coating/interlayer/substrate systems through a micropillar testing protocol, *J. Mater. Res.* 32 (2017) 1421–1431, <https://doi.org/10.1557/jmr.2016.516>.
- [45] C. Shih, Y. Katoh, K.J. Leonard, H. Bei, E. Lara-Curzio, Determination of interfacial mechanical properties of ceramic composites by the compression of micro-pillar test specimens, *J. Mater. Sci.* 48 (2013) 5219–5224, <https://doi.org/10.1007/s10853-013-7311-z>.
- [46] K. Akiyama, E. Nakamura, I. Suzuki, T. Oshika, A. Nishiyama, Y. Sawada, A study of the adhesion between CVD layers and a cemented carbide substrate by AEM analysis, *Surf. Coat. Technol.* 94 (1997) 328–332.
- [47] H.O. Pierson, Fundamentals of chemical vapor deposition, *Handb. Chem. Vap. Depos. CVD*, second ed. Park Ridge: Noyes Publications, USA 1999, pp. 36–58.
- [48] S. Takatsu, K. Shibuki, Diffusion of cobalt into a TiC layer during chemical vapour deposition and its effects on the cutting performance of TiC/Al<sub>2</sub>O<sub>3</sub>-coated cemented carbides, *Thin Solid Films* 127 (1985) 283–292.